SCIENTIFIC REP{O}RTS

OPEN

Enhanced superconductivity in aluminum-based hyperbolic metamaterials

Vera N. Smolyaninova[1], Christopher Jensen[1], William Zimmerman[1], Joseph C. Prestigiacomo[2], Michael S. Osofsky[2], Heungsoo Kim[2], Nabil Bassim[2], Zhen Xing[3], Mumtaz M. Qazilbash[3] & Igor I. Smolyaninov[4]

One of the most important goals of condensed matter physics is materials by design, i.e. the ability to reliably predict and design materials with a set of desired properties. A striking example is the deterministic enhancement of the superconducting properties of materials. Recent experiments have demonstrated that the metamaterial approach is capable of achieving this goal, such as tripling the critical temperature T_C in Al-Al$_2$O$_3$ epsilon near zero (ENZ) core-shell metamaterial superconductors. Here, we demonstrate that an Al/Al$_2$O$_3$ hyperbolic metamaterial geometry is capable of a similar T_C enhancement, while having superior transport and magnetic properties compared to the core-shell metamaterial superconductors.

One of the most important goals of condensed matter physics is reliably designing new materials with enhanced superconducting properties. Recently, a metamaterial strategy, consisting of deliberately engineering the dielectric properties of a nanostructured "metamaterial superconductor" that results in an enhanced electron pairing interaction that increases the value of the superconducting energy gap and the critical temperature, T_c, was suggested to achieve this goal[1,2]. Our recent experimental work[3,4] has conclusively demonstrated that this approach can indeed be used to increase the critical temperature of a composite superconductor-dielectric metamaterial. For example, we have demonstrated the use of Al$_2$O$_3$-coated aluminum nanoparticles to form epsilon near zero (ENZ) core-shell metamaterial superconductors with a T_c that is three times that of pure aluminum[4]. However, this core-shell metamaterial superconductor geometry exhibits poor transport properties compared to its parent (aluminum) superconductor. A natural way to overcome this issue is the implementation of the hyperbolic metamaterial geometry (Fig. 1a), which has been suggested in refs 1,2. Hyperbolic metamaterials are extremely anisotropic uniaxial materials, which behave like a metal ($\mathrm{Re}\varepsilon_{xx} = \mathrm{Re}\varepsilon_{yy} < 0$) in one direction and like a dielectric ($\mathrm{Re}\varepsilon_{zz} > 0$) in the orthogonal direction. Originally introduced to overcome the diffraction limit of optical imaging[5], hyperbolic metamaterials demonstrate a number of novel phenomena resulting from the broadband singular behavior of their density of photonic states. The "layered" hyperbolic metamaterial geometry shown in Fig. 1a is based on parallel periodic layers of metal separated by layers of dielectric. This geometry ensures excellent transport properties in the plane of the layers. As noted in ref. 6, typical high T_c superconductors (such as BSCCO) exhibit hyperbolic behavior in a substantial portion of the far infrared and THz frequency ranges. In this report, we demonstrate that the artificial hyperbolic metamaterial geometry may also lead to a considerable enhancement of superconducting properties.

Electromagnetic properties are known to play a very important role in the pairing mechanism of superconductors[7]. According to the BCS theory, a Cooper pair is formed from two electrons with opposite spins and momenta that are loosely bound. This mechanism may be described as an attractive interaction of electrons that results from the polarization of the ionic lattice which these electrons create as they move through the lattice. Based on this interpretation, Kirzhnits *et al.* formulated their description of superconductivity in terms of the dielectric response function of the superconductor[7]. They demonstrated that the electron-electron interaction in a superconductor may be expressed in the form of an effective Coulomb potential

[1]Department of Physics Astronomy and Geosciences, Towson University, 8000 York Rd., Towson, MD 21252, USA. [2]Naval Research Laboratory, Washington, DC 20375, USA. [3]Department of Physics, College of William and Mary, Williamsburg, Virginia 23187-8795, USA. [4]Department of Electrical and Computer Engineering, University of Maryland, College Park, MD 20742, USA. Correspondence and requests for materials should be addressed to I.I.S. (email: smoly@umd.edu)
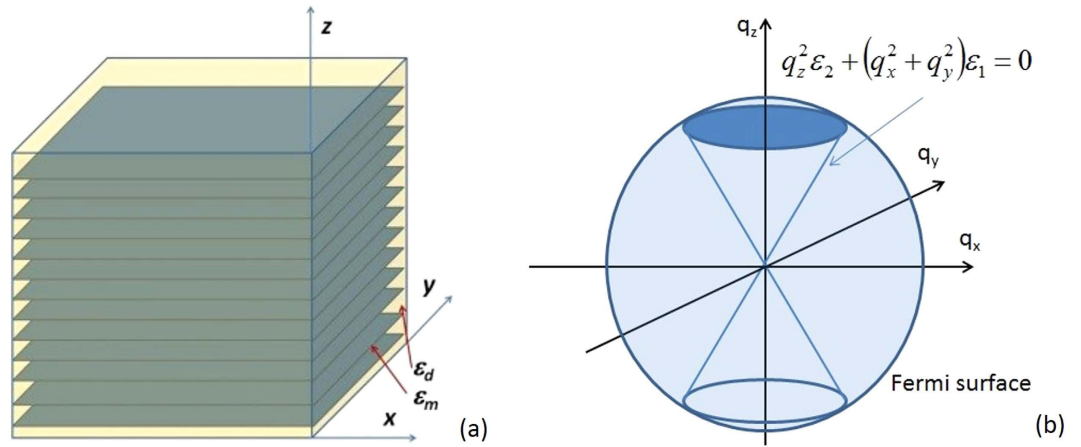
Figure 1. Geometry and basic properties of hyperbolic metamaterial superconductors: (**a**) Schematic geometry of a "layered" hyperbolic metamaterial. (**b**) Electron-electron pairing interaction in a hyperbolic metamaterial is strongly enhanced near the cone in momentum space defined as $q_z^2\varepsilon_2 + \left(q_x^2 + q_y^2\right)\varepsilon_1 = 0$.

$$V(\vec{q}, \omega) = \frac{4\pi e^2}{q^2\varepsilon_{eff}(\vec{q}, \omega)} = V_C\frac{1}{\varepsilon_{eff}(\vec{q}, \omega)} \tag{1}$$

where V_C is the Fourier-transformed Coulomb potential in vacuum, and $\varepsilon_{eff}(q, \omega)$ is the linear dielectric response function of the superconductor treated as an effective medium. Following this "macroscopic electrodynamics" formalism, it appears natural to use the recently developed plasmonics[8] and electromagnetic metamaterial[9] tools to engineer and maximize the electron pairing interaction (Eq. 1) in an artificial "metamaterial superconductor" via deliberate engineering of its dielectric response function $\varepsilon_{eff}(q, \omega)$. For example, it was predicted in refs 1,2 that considerable enhancement of the attractive electron-electron interaction may be expected in such actively studied metamaterial scenarios as ENZ[10] and hyperbolic metamaterials[5]. In both cases $\varepsilon_{eff}(q, \omega)$ may become small and negative in substantial portions of the relevant four-momentum (q, ω) space leading to an enhancement of the electron pairing interaction. Indeed, it was demonstrated in refs 1,2 that in the case of a hyperbolic metamaterial the effective Coulomb potential from Eq. (1) assumes the form

$$V(\vec{q}, \omega) = \frac{4\pi e^2}{q_z^2\varepsilon_2(\vec{q}, \omega) + \left(q_x^2 + q_y^2\right)\varepsilon_1(\vec{q}, \omega)} \tag{2}$$

where $\varepsilon_{xx} = \varepsilon_{yy} = \varepsilon_1$ and $\varepsilon_{zz} = \varepsilon_2$ have opposite signs. As a result, the effective Coulomb interaction of two electrons may become attractive and very strong along spatial directions where

$$q_z^2\varepsilon_2(\vec{q}, \omega) + \left(q_x^2 + q_y^2\right)\varepsilon_1(\vec{q}, \omega) \approx 0 \tag{3}$$

Demonstration of the resulting superconductivity enhancement in hyperbolic metamaterials would open up numerous new possibilities for metamaterial enhancement of T_c in such practically important simple superconductors as niobium and MgB$_2$.

Here, we report the first successful realization of such an artificial hyperbolic metamaterial superconductor, which is made of aluminum films separated by thin layers of Al$_2$O$_3$. This combination of materials is ideal for the proof of principle experiments because it is easy to controllably grow Al$_2$O$_3$ on the surface of Al, and because the critical temperature of aluminum is quite low ($T_{c\,Al} = 1.2\,\text{K}$[11]), leading to a very large superconducting coherence length $\xi = 1600\,\text{nm}$[11]. Such a large value of ξ facilitates the metamaterial fabrication requirements since the validity of macroscopic electrodynamic description of the metamaterial superconductor requires that its spatial structural parameters must be much smaller than ξ. It appears that the Al/Al$_2$O$_3$ hyperbolic metamaterial geometry is capable of superconductivity enhancement, which is similar to that observed for a core-shell metamaterial geometry[4], while having much better transport and magnetic properties compared to the core-shell superconductors. The multilayer Al/Al$_2$O$_3$ hyperbolic metamaterial samples for our experiments (Fig. 2) were prepared using sequential thermal evaporation of thin aluminum films followed by oxidation of the top layer for 1 hour in air at room temperature. The first layer of aluminum was evaporated onto a glass slide surface. Upon exposure to ambient conditions a $\sim$2 nm thick Al$_2$O$_3$ layer is known to form on the aluminum film surface[12]. Further aluminum oxidation may also be achieved by heating the sample in air. The oxidized aluminum film surface was used as a substrate for the next aluminum layer. This iterative process was used to fabricate thick multilayer (up to 16 metamaterial layers) Al/Al$_2$O$_3$ hyperbolic metamaterial samples (throughout our paper a single metamaterial layer is understood as a layer of Al with a layer of Al$_2$O$_3$ on its top surface). A transmission electron microscope (TEM) image of the multilayer metamaterial sample is shown in Fig. 2. During TEM experiments samples were coated with gold and platinum to ensure conductivity of the surface during sample preparation. A focused ion
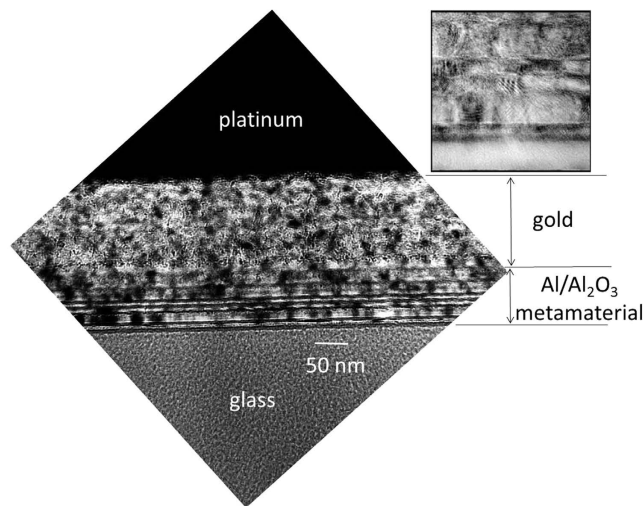
Figure 2. Transmission electron microscope (TEM) image of a 16 layer metamaterial sample. During the imaging experiments samples were coated with gold and platinum to ensure conductivity of the surface during sample preparation. The inset shows that the interfacial layers are amorphous, between polycrystalline grains of Al, that, in cross-section, exhibit Moire cross-hatching.

beam (FIB) microscope was used to prepare a sample for transmission electron microscopy (TEM). Samples were analyzed using a JEOL 2200 FS TEM, acquiring bright field and high resolution images. Figure 2 shows an image from the hyperbolic stack, showing polycrystalline Al grains, with 1–2 nm thick amorphous Al_2O_3 spacing layers, corresponding with the designed structure. Some Al_2O_3 layers are difficult to discern due to slight sample warping from the preparation process. The inset shows that the interfacial layers are indeed amorphous, between polycrystalline grains of Al, that, in cross-section, exhibit Moire cross-hatching.

To demonstrate that our multilayer samples exhibit hyperbolic behavior, we studied their transport and optical properties (Figs 3,4 and 5). The temperature dependences of the sheet resistance of a 16-layer 10 nm/layer Al/ Al_2O_3 hyperbolic metamaterial and a 100 nm thick Al film are shown in Fig. 3a. As illustrated in the logarithmic plot in the inset, the electronic conductivity of the metamaterial approaches conductivity values of bulk aluminum (indicated by the arrow), and is far removed from the parameter space characteristic for granular Al films[13], which is indicated by the gray area in the inset. These results were corroborated by measurements of IR reflectivity of these samples, shown in Fig. 3b. The IR reflectivity of the hyperbolic metamaterial samples was measured in the long wavelength IR (LWIR) (2.5–22.5 μm) range using an FTIR spectrometer, and compared with reflectivity spectra of Al and Al_2O_3. While the reflectivity spectrum of bulk Al is almost flat, the spectrum of Al_2O_3 exhibits a very sharp step-like behavior around 11 μm that is related to the phonon-polariton resonance, which results from coupling of an infrared photon with an optical phonon of Al_2O_3[14]. The step in reflectivity is due to the negative sign of ε_{Al2O3} near the resonance. The absence of this step in our multilayers indicates that the aluminum layers in our samples are continuous and not intermixed with aluminum oxide. Such a step is clearly observed in reflectivity data obtained from a core-shell Al/Al_2O_3 sample shown in Fig. 3b where the aluminum grains are separated from each other by Al_2O_3. On the other hand, this step is completely missing in reflectivity spectra of the hyperbolic metamaterial samples (the step at 9 μm observed in the spectrum of a three-layer sample is due to phonon-polariton resonance of the SiO_2 substrate). Thus, our transport and optical measurements confirm excellent DC and AC (optical) conductivity of the aluminum layers of the fabricated hyperbolic metamaterials.

The Kramers-Kronig analysis of the FTIR reflectivity spectra of Al and Al_2O_3 measured in ref. 4 also allowed us to calculate the ε_1 and ε_2 components of the Al/Al_2O_3 layered films in the LWIR spectral range using the Maxwell-Garnett approximation as follows:

$$\varepsilon_1 = n\varepsilon_m + (1 - n)\varepsilon_d \tag{4}$$

$$\varepsilon_2 = \frac{\varepsilon_m\varepsilon_d}{(1 - n)\varepsilon_m + n\varepsilon_d} \tag{5}$$

where n is the volume fraction of metal, and ε_m and ε_d are the dielectric permittivities of the metal and dielectric, respectively[15]. Results of these calculations for a multilayer metamaterial consisting of 13 nm thick Al layers separated by 2 nm of Al_2O_3 are shown in Fig. 4. The metamaterial appears to be hyperbolic except for a narrow LWIR spectral band between 11 and 18 μm. A good match between the Maxwell-Garnett approximation (Equations (4 and 5)) and the measured optical properties of the metamaterial is demonstrated by ellipsometry (Fig. 5a) and polarization reflectometry (Fig. 5b) of the samples.

Variable angle spectroscopic ellipsometry with photon energies between 0.6 eV and 6.5 eV on the Al/Al_2O_3 metamaterial have been performed using a Woollam Variable Angle Spectroscopic Ellipsometer (W-VASE). For a uniaxial material with optic axis perpendicular to the sample surface and in plane of incidence, ellipsometry
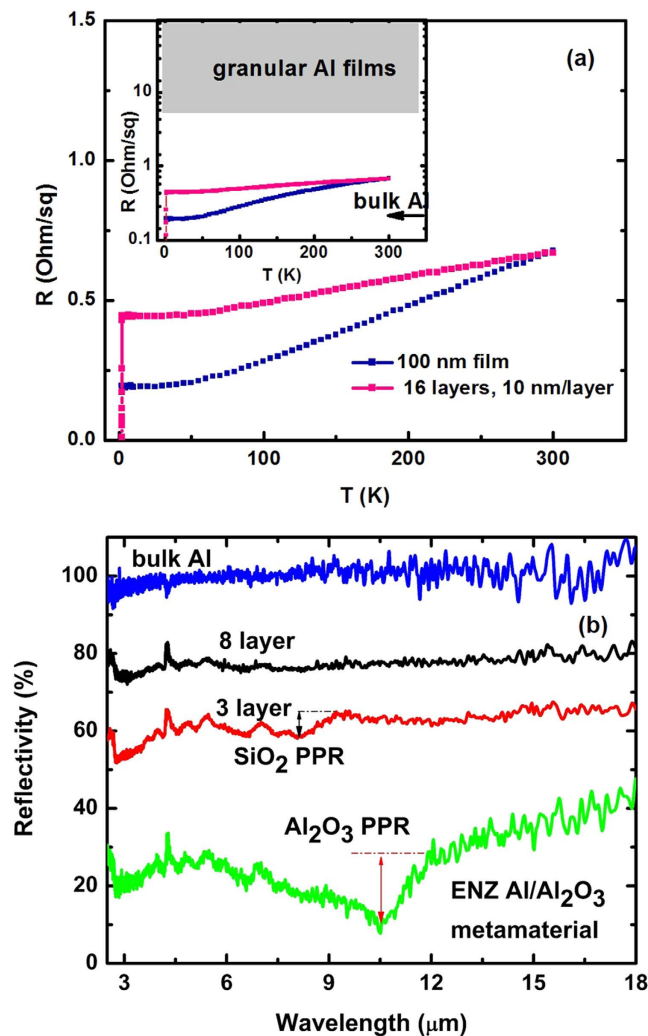
Figure 3. Measurements of DC and AC (optical) conductivity of the aluminum layers of the fabricated hyperbolic metamaterials: (**a**) Temperature dependences of the sheet resistance of a 16-layer 10 nm/layer Al/ Al$_2$O$_3$ hyperbolic metamaterial and a 100 nm thick Al film. As illustrated in the logarithmic plot in the inset, the conductivity of the metamaterial approaches conductivity values of bulk aluminum and is far removed from the parameter space characteristic for granular Al films which is indicated by the gray area. (**b**) IR reflectivity of bulk aluminium, 3 and 8 layer hyperbolic metamaterial, and the core shell metamaterial samples measured in the long wavelength IR (LWIR) (2.5–22.5 μm) range using an FTIR spectrometer. The step in reflectivity around 11 μm is related to the phonon-polariton resonance (PPR) and may be used to characterize the spatial distribution of Al$_2$O$_3$ in the metamaterial samples.

provides the pseudo-dielectric function which, in general, depends both on ε_1 and ε_2. However, as demonstrated by Jellison and Baba[16], the pseudo-dielectric function in this measurement geometry is dominated by the in-plane dielectric function ε_1 and is independent of the angle of incidence. We find that the pseudo-dielectric function of the Al/Al$_2$O$_3$ metamaterial is indeed similar (but not the same) as that of aluminum i.e. metallic as expected from effective medium theory. We also find that the pseudo-dielectric function is rather insensitive to the angle of incidence. The measured results for the real and imaginary parts of the pseudo-dielectric function in Fig. 5a show good agreement with the model for the in-plane dielectric function (Equation (4)). The calculated data points are based on the real and imaginary parts of ε_{Al} tabulated in ref. 17. The measured sign of the real part of the pseudo-dielectric function is negative, which suggests metallic in-plane transport. The sign of the real part of ε_2 (and therefore, the hyperbolic character of our samples) was determined by polarization reflectometry, since ellipsometry data are less sensitive to ε_2[16]. Polarization reflectometry also confirmed the negative sign of the real part of ε_1 consistent with ellipsometry data. The metamaterial parameters were extracted from the polarization reflectometry data as described in detail in ref. 18. Reflectivity for s-polarization is given in terms of the incident angle θ by

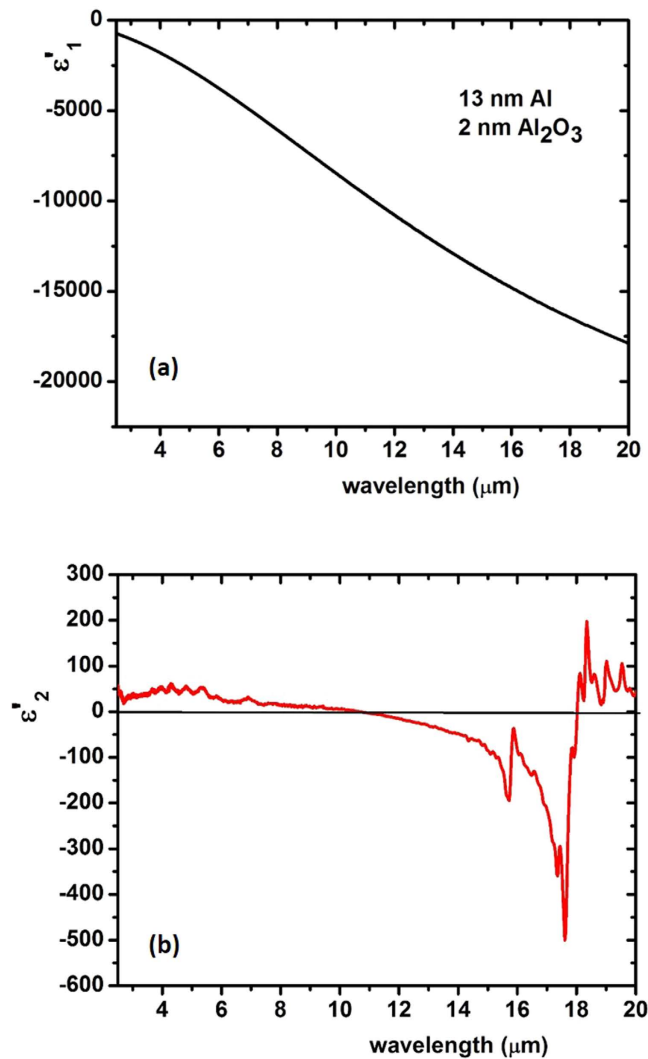$$R_s = \left| \frac{\sin(\theta - \theta_{ts})}{\sin(\theta + \theta_{ts})} \right|^2,$$

(6)

Figure 4. The calculated plots of the real parts of $\varepsilon_{x,y}$ (**a**) and ε_z (**b**) of the multilayer Al/Al$_2$O$_3$ metamaterial. The metamaterial consists of 13 nm thick Al layers separated by 2 nm of Al$_2$O$_3$ in the LWIR spectral range. The calculations were performed using Eqs (4 and 5) based on the Kramers-Kronig analysis of the FTIR reflectivity of Al and Al$_2$O$_3$ in ref. 4. The metamaterial appears to be hyperbolic except for a narrow LWIR spectral band between 11 and 18 μm.

where

$$\theta_{ts} = \arcsin\left(\frac{\sin\theta}{\sqrt{\varepsilon_1}}\right).$$

(7)

Reflectivity for p-polarization is given as

$$R_p = \left|\frac{\varepsilon_1 \tan\theta_{tp} - \tan\theta}{\varepsilon_1 \tan\theta_{tp} + \tan\theta}\right|^2$$

(8)

where

$$\theta_{tp} = \arctan\sqrt{\frac{\varepsilon_2 \sin^2\theta}{\varepsilon_1\varepsilon_2 - \varepsilon_1 \sin^2\theta}}.$$

(9)

We measured p- and s- polarized absolute reflectance on the metamaterial sample using the reflectance mode of the ellipsometer. The reflectance was measured at two photon energies, 2.07 eV (600 nm) and 2.88 eV (430 nm), as shown in Fig. 5b and was normalized to the measured reflectance of a 150 nm gold film. The absolute reflectance of the gold film was obtained from ellipsometry measurements. The estimated uncertainty in the absolute
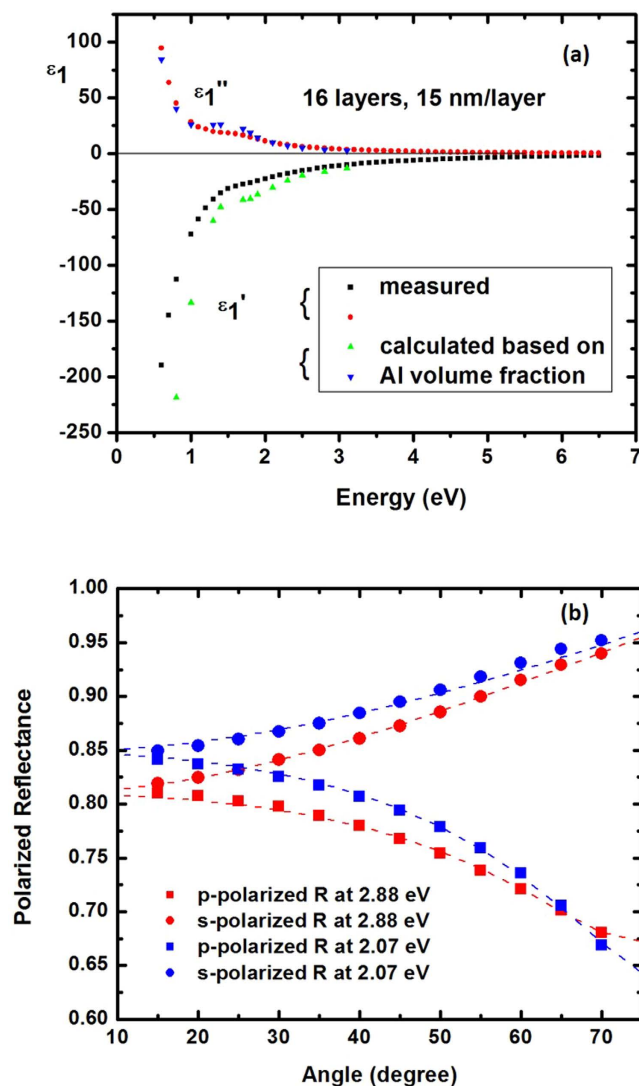
Figure 5. Ellipsometry and polarization reflectometry of Al/Al$_2$O$_3$ hyperbolic metamaterials. (a) Comparison of measured pseudo-dielectric function using ellipsometry and theoretically calculated Reε_1 and Imε_1. Theoretical data points are based on real and imaginary parts of ε_{Al} tabulated in ref. 17. **(b)** Data points are measured p- and s-polarized reflectivities of the metamaterial sample at 2.07 eV (600 nm) and 2.88 eV (430 nm). Dashed lines are fits using Eqs (6–9). ε_1 and ε_2 obtained from the fits confirm hyperbolic character of the metamaterial.

reflectance of the Al/Al$_2$O$_3$ metamaterial is one percent. In order to obtain the dielectric permittivity ε_1 and ε_2 values, we fit the s- polarized reflectance first, and get the in-plane dielectric function ε_1. We then use the in-plane dielectric function to fit the p- polarized reflectance to obtain the out-of-plane dielectric function, ε_2. The data analysis was done using W-VASE software. At 2.07 eV (600 nm), $\varepsilon_1 = -7.17 + 1.86i$ and $\varepsilon_2 = 1.56 + 0.21i$, and at 2.88 eV (430 nm), $\varepsilon_1 = -2.15 + 0.50i$ and $\varepsilon_2 = 1.30 + 0.09i$. It is clear that the real part of the out-of-plane dielectric function is positive while the real part of the in-plane dielectric function is negative, which confirms the dielectric nature along z-axis and metallic nature in the xy-plane i.e. a hyperbolic metamaterial.

The T_c and critical magnetic field, H_c, of various samples (Figs 6 and 7) were determined via four-point resistivity measurements as a function of temperature and magnetic field, H, using a Physical Property Measurement System (PPMS) by Quantum Design. Even though the lowest achievable temperature with our PPMS system was 1.75 K, which is higher than the critical temperature $T_{cAl} = 1.2$ K of bulk aluminum, we were able to observe a pronounced effect of the number of layers on T_c of the hyperbolic metamaterial samples. Figure 6a shows measured resistivity as a function of temperature for the 1-layer, 3-layer and 8-layer samples each having the same 8.5 nm layer thickness. While the superconducting transition in the 1-layer sample was below 1.75 K, and could not be observed, the 3-layer and 8-layer metamaterial samples exhibited progressively higher critical temperature, which strongly indicates the role of hyperbolic geometry in T_c enhancement. A similar set of measurements performed for several samples having 13 nm layer thickness is shown in Fig. 6b.
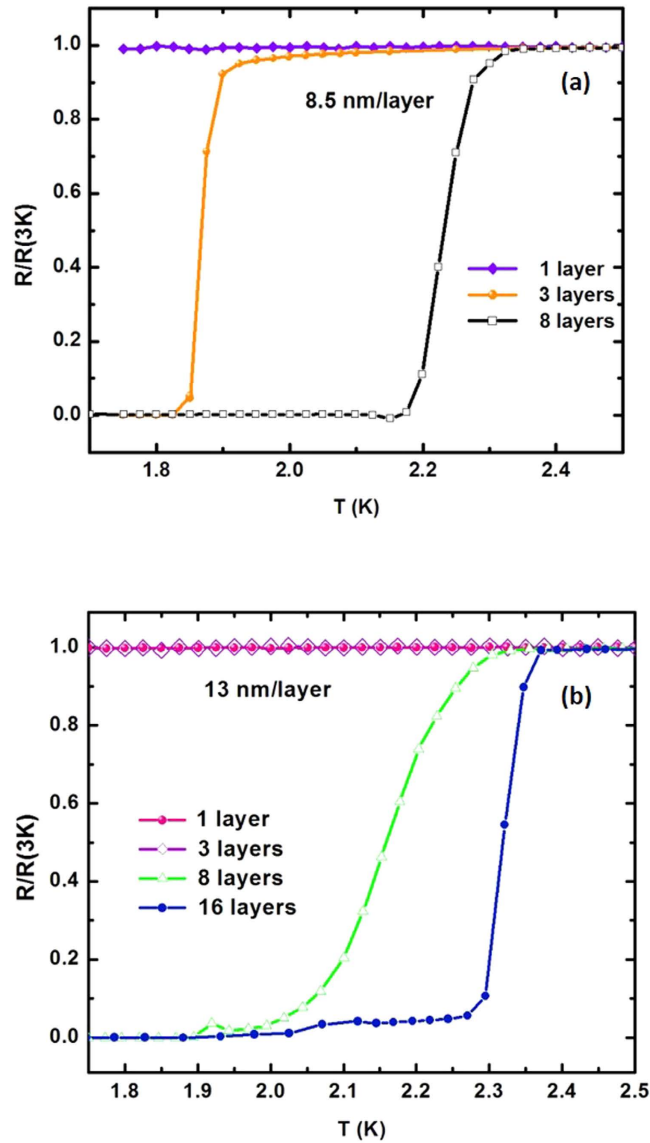
Figure 6. Effect of the number of layers on T_c of the Al/Al$_2$O$_3$ hyperbolic metamaterial samples: (**a**) Measured resistivity as a function of temperature is shown for the 1-layer, 3-layer and 8-layer samples each having the same 8.5 nm layer thickness. (**b**) Measured resistivity as a function of temperature for the 1-layer, 3-layer, 8-layer and 16-layer samples each having the same 13 nm layer thickness.

The measurements of H_c in parallel and perpendicular fields are shown in Fig. 7. Figure 7a shows measured resistivity as a function of temperature for a 16-layer 13.2 nm layer thickness hyperbolic metamaterial sample. The critical temperature of this sample appears to be $T_c = 2.3$ K, which is about two times higher than the T_c of bulk aluminum (another transition at $T_c = 2.0$ K probably arise from one or two decoupled layers or edge shadowing effects where the thickness of the films is not uniform). The inset in Fig. 7a illustrates the measurements of $H_c^{parallel}$ for this sample. The critical field appears to be quite large ($\sim$3T), which is similar to the values of $H_c^{parallel}$ observed previously in granular aluminium films[19]. However, it is remarkable that such high critical parameters are observed for the films, which are much thicker than granular Al films.

Measurements of the perpendicular critical field H_c^{perp} for the same metamaterial sample, which are shown in Fig. 7b allowed us to evaluate the Pippard coherence length

$$\xi = \sqrt{\frac{\phi_0}{2\pi H_{c2}}}$$

(10)

Assuming $H_{c2}^{perp} = 100$ G (based on the inset in Fig. 7b) the corresponding coherence length appears to be $\xi = 181$ nm, which is much larger than the layer periodicity. Other measured samples also exhibit the coherence length around 200 nm. Therefore, our use of effective medium approach is validated and our multilayer samples should obey the metamaterial theory.
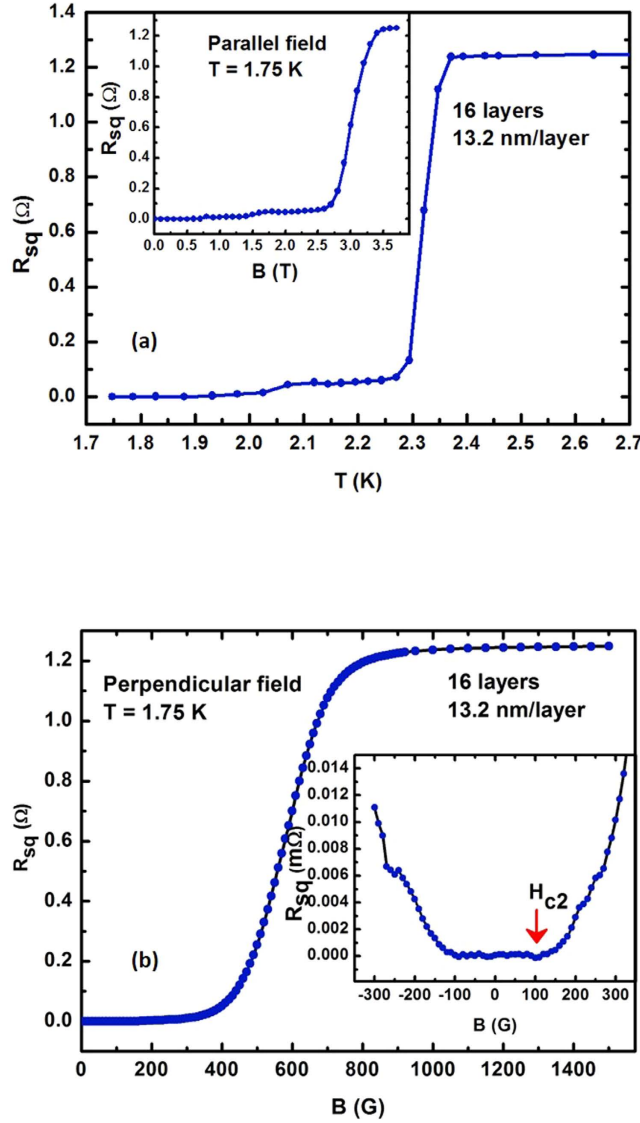
Figure 7. Evaluation of the Pippard coherence length of the Al/Al$_2$O$_3$ hyperbolic metamaterial: (**a**) Measured resistivity as a function of temperature for a 16-layer 13.2 nm layer thickness metamaterial sample. The critical temperature appears to be T$_c$ = 2.3 K. The inset shows resistivity of this sample as a function of parallel magnetic field at T = 1.75 K. (**b**) Resistivity of the same sample as a function of perpendicular magnetic field at T = 1.75 K. Assuming H$_{c2}^{perp}$ = 100G (based on the measurements shown in the inset) the corresponding coherence length appears to be ξ = 181 nm, which is much larger than the layer periodicity.

We have also studied changes in T_c as a function of Al layer thickness in a set of several 8-layer Al/Al$_2$O$_3$ metamaterial samples, as shown in Fig. 8a. The quantitative behaviour of T_c as a function of n may be predicted based on the hyperbolic enhancement of the electron-electron interaction (Eq. (2)) and the density of electronic states, ν on the Fermi surface which experience this hyperbolic enhancement. Using Eqs (4 and 5), the effective Coulomb potential from Eq. (2) may be re-written as

$$V(\vec{q}, \omega) = \frac{4\pi e^2}{q^2 \left[\frac{q_z^2}{q^2} \frac{\varepsilon_d \varepsilon_m}{((1-n)\varepsilon_m + n\varepsilon_d)} + \frac{q_x^2 + q_y^2}{q^2} (n\varepsilon_m + (1-n)\varepsilon_d) \right]}.$$

(11)

Let us assume that the dielectric response function of the metal used to fabricate the hyperbolic metamaterial shown in Fig. 1 may be written as

$$\varepsilon_m(q, \omega) = \left(1 - \frac{\omega_p^2}{\omega^2 - \omega_p^2 q^2/k^2} \right) \left(1 - \frac{\Omega_1^2(q)}{\omega^2} \right) \cdots \left(1 - \frac{\Omega_n^2(q)}{\omega^2} \right)$$
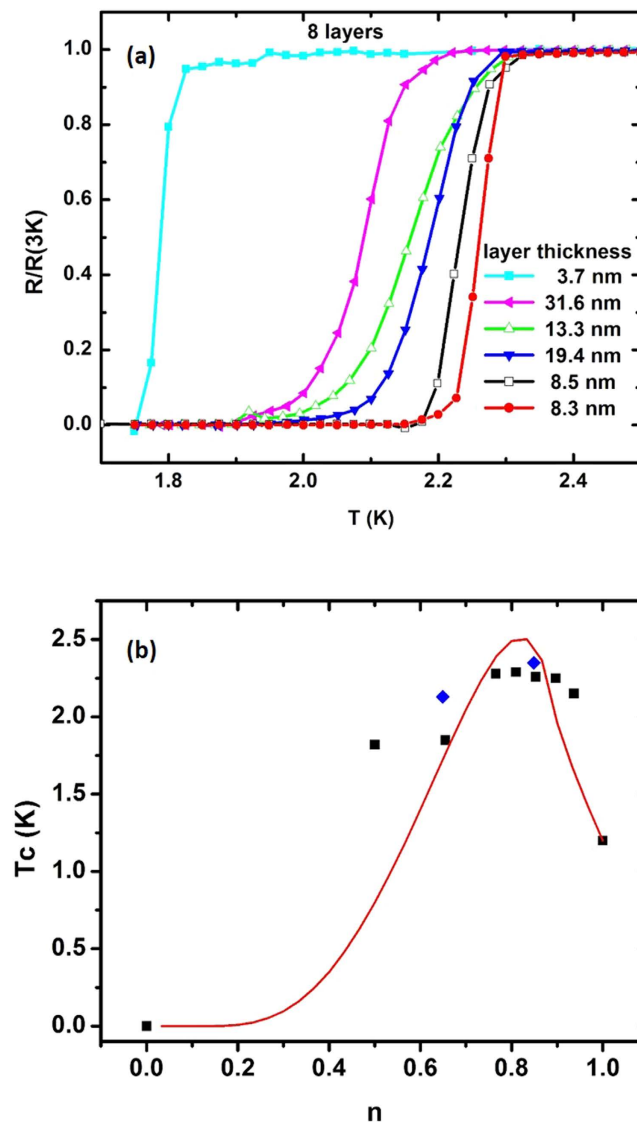
(12)

Figure 8. Effect of the aluminum volume fraction n on T_c of the Al/Al$_2$O$_3$ hyperbolic metamaterial samples: (**a**) Resistivity as a function of temperature for the 8-layer samples having different aluminum layer thicknesses. (**b**) Experimentally measured behavior of T_c as a function of n (which is defined by the Al layer thickness) correlates well with the theoretical fit (red curve) based on the hyperbolic mechanism of T_c enhancement. Experimental data points shown in black correspond to 8-layer samples, while blue ones correspond to 16-layer samples.

where ω_p is the plasma frequency, k is the inverse Thomas-Fermi radius, and $\Omega_n(q)$ are dispersion laws of various phonon modes[20]. Zeroes of the dielectric response function $\varepsilon_m(q, \omega)$ of the bulk metal (which correspond to its various bosonic modes) maximize the electron-electron pairing interaction given by Eq. (1). As summarized in ref. 21, the critical temperature of a superconductor is typically calculated as

$$T_c = \theta \, \exp\left(-\frac{1}{\lambda_{eff}}\right),$$

(13)

where θ is the characteristic temperature for a bosonic mode mediating the electron pairing interaction (such as the Debye temperature θ_D in the standard BCS theory), and λ_{eff} is the dimensionless coupling constant defined by $V(q, \omega) = V_C(q)\varepsilon^{-1}(q, \omega)$ and the density of states ν (see for example ref. 22):

$$\lambda_{eff} = -\frac{2}{\pi}\nu \int_0^\infty \frac{d\omega}{\omega} \langle V_C(q)\text{Im}\,\varepsilon^{-1}(\vec{q}, \omega)\rangle,$$

(14)

where V_C is the unscreened Coulomb repulsion. The integral in Eq. (14) is typically simplified to take into account only the contributions from the poles of the inverse dielectric response function $\varepsilon^{-1}(q, \omega)$, while averaging is performed over all the spatial directions.

Let us consider the region of four-momentum (q, ω) space, where $\omega > \Omega_1(q)$. While $\varepsilon_m = 0$ at $\omega = \Omega_1(q)$, $\varepsilon_m(q, \omega)$ is large in a good metal and negative just above $\Omega_1(q)$. Compared to the bulk metal, the poles of the angular-dependent νV product of the hyperbolic metamaterial are observed at shifted positions compared to the zeroes of ε_m, and additional poles may also appear[2]. Based on Eq. (11), the differential of the product νV may be written as

$$d(\nu V) = \frac{4\pi e^2 n \ \sin\theta d\theta}{q^2 \left(\frac{\varepsilon_d \varepsilon_m}{((1-n)\varepsilon_m + n\varepsilon_d)} \cos^2\theta + (n\varepsilon_m + (1-n)\varepsilon_d)\sin^2\theta \right)}$$

$$= -\frac{4\pi e^2 n dx}{q^2 \left((n\varepsilon_m + (1-n)\varepsilon_d) - \frac{n(1-n)(\varepsilon_m - \varepsilon_d)^2}{(n\varepsilon_d + (1-n)\varepsilon_m)} x^2 \right)},$$

(15)

where $x = \cos\theta$, and θ varies from 0 to π. The latter expression has two poles at

$$\varepsilon_m = \left(\left(1 - \frac{1}{2n(1-n)(1-x^2)} \right) \pm \sqrt{\left(1 - \frac{1}{2n(1-n)(1-x^2)} \right)^2 - 1} \right) \varepsilon_d$$

(16)

As the volume fraction, n, of metal is varied, one of these poles remains close to $\varepsilon_m = 0$, while the other is observed at larger negative values of ε_m:

$$\varepsilon_m^+ \approx -n(1-n)(1-x^2)\varepsilon_d$$

(17)

$$\varepsilon_m^- \approx -\frac{\varepsilon_d}{n(1-n)(1-x^2)}$$

(18)

This situation is similar to calculations of T_c for ENZ metamaterials[23]. Since the absolute value of ε_m is limited (see Eq. (12)), the second pole disappears near $n = 0$ and near $n = 1$. Due to the complicated angular dependences in Eq. (16), it is convenient to reverse the order of integration in Eq. (14), and perform the integration over $d\omega$ first, followed by angular averaging. Following the commonly accepted approach, while integrating over $d\omega$ we take into account only the contributions from the poles given by

Equation (16), and assume the value of $\text{Im}\varepsilon_m = \varepsilon_m''$ to be approximately the same at both poles. The respective contributions of the poles to $d(\nu V)/dx$ may be written as

$$\frac{d(\nu V)}{dx} \approx \frac{2\pi e^2 \left[(1-n)\left(\left(1 - \frac{1}{2n(1-n)(1-x^2)} \right) \pm \sqrt{\left(1 - \frac{1}{2n(1-n)(1-x^2)} \right)^2 - 1} \right) + n \right]}{q^2 \varepsilon''_m (1-n)(1-x^2) \sqrt{\left(1 - \frac{1}{2n(1-n)(1-x^2)} \right)^2 - 1}}$$

(19)

Near $n = 0$ and $n = 1$ these expression may be approximated as

$$\frac{d(\nu V)^+}{dx} \approx \frac{4\pi e^2 n^2}{q^2 \varepsilon''_m}$$

(20)

and

$$\frac{d(\nu V)^-}{dx} \approx \frac{4\pi e^2}{q^2 \varepsilon''_m (1-x^2)},$$

(21)

respectively. Note that at the $\omega = \Omega_1(q)$ zero of the dielectric response function of the bulk metal the effective Coulomb potential inside the metal may be approximated as

$$V_m(\vec{q}, \omega) = \frac{4\pi e^2}{q^2 \varepsilon_m(q, \omega)} \approx -\frac{4\pi e^2}{q^2 \varepsilon''_m},$$

(22)

so that the coupling constant λ_{eff} of the hyperbolic metamaterial obtained by angular integration of the sum of Eqs (20) and (21) may be expressed via the coupling constant λ_m of the bulk metal:

$$\lambda_{eff} \approx \lambda_m \left(n^2 + \alpha \ \ln\left| \frac{1 + x_0}{1 - x_0} \right| \right),$$

(23)

where α is a constant of the order of 1 and x_0 is defined by the maximum negative value of ε_m, which determines if the second pole (Equation (18)) exists at a given n. Based on Eq. (18),

$$x_0^2 \approx 1 + \frac{\varepsilon_d}{n(1-n)\varepsilon_{m,\max}}$$

(24)

If the second pole does not exist then $x_0 = 0$ may be assumed. Based on Eq. (13), the theoretically predicted value of T_c for the hyperbolic metamaterial is calculated as

$$T_c = T_{Cbulk} \exp\left(\frac{1}{\lambda_m} - \frac{1}{\lambda_{eff}}\right) = T_{Cbulk} \exp\left(\frac{1}{\lambda_m}\left(1 - \frac{1}{n^2 + \alpha \ \ln\left|\frac{1+x_0}{1-x_0}\right|}\right)\right)$$

(25)

assuming the known values $T_{cbulk} = 1.2$ K and $\lambda_m = 0.17$ for bulk aluminum[23]. The predicted behaviour of T_c as a function of n is plotted in Fig. 8b. This figure demonstrates that the experimentally measured behaviour of T_c as a function of n (which is defined by the Al layer thickness) correlates well with the theoretical fit, which was obtained using Eq. (25) based on the hyperbolic mechanism of T_c enhancement.

The observed combination of transport and critical properties of the Al/Al_2O_3 hyperbolic metamaterials is very far removed from the parameter space typical of the granular aluminum films[13,19]. Together with the number of layer and layer thickness dependences of T_c and H_c shown in Figs 6,7 and 8, these observations strongly support the hyperbolic metamaterial mechanism of superconductivity enhancement described by Eqs (11–25). The developed technology enables efficient nanofabrication of thick film aluminum-based hyperbolic metamaterial superconductors with a T_c that is two times that of pure aluminum and with excellent transport and magnetic properties. While the observed T_c increase is slightly smaller than the one observed in ENZ metamaterials[4], the hyperbolic metamaterial geometry exhibits superior transport and magnetic properties compared to the ENZ core-shell metamaterial superconductors. In addition, our theoretical model is applicable to previous experiments performed in NbN/AlN[24] and Al/Si[25] multilayer geometries. We should also note that unlike recent pioneering work on quantum metamaterials[26], which are based on superconducting split-ring resonators and quantum circuits, our work aims at engineering of metamaterials with enhanced superconducting properties.

Our results open up numerous new possibilities for considerable T_c enhancement in other practically important simple superconductors, such as niobium and MgB_2. However, due to their much smaller coherence length[11,20] metamaterial structuring of these superconductors must be performed on a much more refined scale. The two-fold increase of T_c in an artificial hyperbolic metamaterial superconductor that we have observed suggests that the recently discovered hyperbolic properties of high T_c superconductors (such as BSCCO)[6] may play a considerable role in the high values of T_c observed in cuprates.

References

1. Smolyaninov, I. I. & Smolyaninova, V. N. Is there a metamaterial route to high temperature superconductivity? *Adv. Cond. Matt. Phys.* **2014,** 479635 (2014).
2. Smolyaninov, I. I. & Smolyaninova, V. N. Metamaterial superconductors. *Phys. Rev. B* **91,** 094501 (2015).
3. Smolyaninova, V. N. *et al.* Experimental demonstration of superconducting critical temperature increase in electromagnetic metamaterials. *Scientific Reports* **4,** 7321 (2014).
4. Smolyaninova, V. N. *et al.* Using metamaterial nanoengineering to triple the superconducting critical temperature of bulk aluminum. *Scientific Reports* **5,** 15777 (2015).
5. Jakob, Z., Alekseyev, L. V. & Narimanov, E. Optical hyperlens: far-field imaging beyond the diffraction limit. *Optics Express* **14,** 8247 (2006).
6. Smolyaninov, I. I. Quantum topological transition in hyperbolic metamaterials based on high Tc superconductors. *Journal of Physics: Condensed Matter* **26,** 305701 (2014).
7. Kirzhnits, D. A., Maksimov, E. G. & Khomskii, D. I. The description of superconductivity in terms of dielectric response function. *J. Low Temp. Phys.* **10,** 79 (1973).
8. Zayats, A. V., Smolyaninov, I. I. & Maradudin, A. Nano-optics of surface plasmon-polaritons. *Physics Reports* **408,** 131 (2005).
9. Pendry, J. B., Schurig, D. & Smith, D. R. Controlling electromagnetic fields. *Science* **312,** 1780 (2006).
10. Engheta, N. Pursuing near-zero response. *Science* **340,** 286 (2013).
11. Kittel, C. *Introduction to Solid State Physics* (Wiley, New York, 2004).
12. Shih T.-S. & Liu, Z.-B. Thermally-formed oxide on aluminum and magnesium. *Materials Transactions* **47,** 1347 (2006).
13. Cohen, R. W. & Abeles, B. Superconductivity in granular aluminum films. *Phys. Rev.* **168,** 444–450 (1968).
14. Mills, D. L. & Burstein, E. Polaritons: the electromagnetic modes of media. *Rep. Prog. Phys.* **37,** 817 (1974).
15. Wangberg, R. *et al.* Nonmagnetic nanocomposites for optical and infrared negative-refractive-index media. *J. Opt. Soc. Am. B* **23,** 498 (2006).
16. Jellison, G. E. & Baba, J. C. Pseudodielectric functions of uniaxial materials in certain symmetry directions. *J. Opt. Soc. Am. A* **23,** 468–475 (2006).
17. Ordal, M. A. *et al.* Optical properties of the metals Al, Co, Cu, Au, Fe, Pb, Ni, Pd, Pt, Ag, Ti, and W in the infrared and far infrared. *Applied Optics* **22,** 1099–1119 (1983).
18. Tumkur, T. *et al.* Permittivity evaluation of multilayered hyperbolic metamaterials: Ellipsometry vs. reflectometry. *J. Appl. Phys.* **117,** 103104 (2015).
19. Prestigiacomo, J. C., Liu, T. J. & Adams, P. W. Asymmetric avalanches in the condensate of a Zeeman-limited superconductor. *Phys. Rev. B* **90,** 184519 (2014).
20. Ashcroft, N. W. & Mermin, N. D. *Solid State Physics* (Saunders, New York, 1976).
21. Ginzburg, V. L. Nobel Lecture: On superconductivity and superfluidity. *Rev. Mod. Phys.* **76,** 981–998 (2004).
22. Pashitskii, E. A. Plasmon mechanism of high temperature superconductivity in cuprate metal-oxide compounds. *JETP* **76,** 425–444 (1993).
23. Smolyaninov, I. I. & Smolyaninova, V. N. Theoretical modeling of critical temperature increase in metamaterial superconductors. *Phys. Rev. B* **93,** 184510 (2016).
24. Barber, Z. H. & Blamire, M. G. Niobium nitride/aluminium nitride superconductor/insulator multilayers and tunnel junctions. *IEEE Trans. on Applied Superconductivity* **7,** 3609–3612 (1997).

25. Tarasov, M. A., Kuzmin, L. S. & Kaurova, N. S. Thin multilayer aluminum structures for superconducting devices. *Instruments and Experimental Techniques* **52,** 877–881 (2009).
26. Macha, P. *et al.* Implementation of a quantum metamaterial using superconducting qubits. *Nature Communications* **5,** 5146 (2014).

Acknowledgements

Author Contributions

I.I.S., V.N.S. and M.S.O. wrote the main manuscript text, V.N.S., C.J. and W.Z. fabricated samples, V.N.S., J.C.P., M.S.O., H.K., N.B., Z.X., M.M.Q. and I.I.S. collected experimental data. All authors discussed and reviewed the manuscript.

Additional Information